ENHANCED UP-CONVERSION AND TEMPERATURE-SENSING BEHAVIOUR OF Er^{3+} AND Yb^{3+} CO-DOPED $Y_2Ti_2O_7$ BY INCORPORATION OF Li^+ IONS

5.1 Introduction

Lanthanide (Ln^{3+})-doped nano-phosphors have attracted much attention because of their wide applicability in optical filters, as laser materials, LEDs, and spectral convertors as the next-generation energy-harvesting materials in solar cells and up-conversion luminescent nano-materials [Shivakumar, et al. (2006), Neccache, et al. (2009), Boyer, et al. (2007), Ende, et al. (2009)]. The interest in nano-phosphors are increasing because of their superior features such as long-lived luminescence, anti-Stokes shifts, narrow emission bands, high resistance to photo-bleaching, remarkable light penetration depth in tissue, and low toxicity compared to conventional molecular probes such as organic dyes and quantum dots [Gupta, et al. (2011)]. Ln^{3+}-doped nano-phosphors involve intra 4f–4f electronic transitions, providing fascinating features because of abundant energy levels with long lifetimes (~ms to μs), parity-forbidden nature of 4f–4f transitions and a sharp spectral width ~10 nm. However, the low absorption cross-section of Ln^{3+} ions often results a low efficiency of luminescence transition on direct excitation into the *4f* bands. To overcome this problem, Yb^{3+} ion has been used as a prominent sensitizer because of its large absorption cross-section at NIR excitation than for Er^{3+} and/or Tm^{3+} ion. Energy is transferred from Yb^{3+} to Er^{3+}/Tm^{3+}. The up-conversion process (two/three-photon process) is observed when subsequent energy transfer (ET) promotes the electrons of Er^{3+} and/or Tm^{3+} ions to higher energy levels, and radiative decay lead to emission of, up-converted photons in the visible range [Dong, et al. (2012)].In particular, the advances in IR sources, the upconverted intense blue-, green-, and red-emitting colour phosphors are available. These phosphors are important in designing smart temperature-sensing devices and bio-imaging applications [Wang, et al. (2010), Chen, et al. (2011), Ansari, et al. (2013). $Y_2Ti_2O_7$, as one of the members of the classical pyrochlore family, has attracted much attention because of its unique optical properties and potential applications in up-conversion lasers, bio-imaging, and DNA detection [Ting, et al. (2011), Singh, et al.

(2013)]. However, the up-conversion efficiency of these nano-crystals is still inadequate, thus limiting their wide applications. Various studies have been performed to enhance the up-conversion intensity by changing the crystal phase, functionalising the surface of the sample, incorporating a co-dopant sensitizer, and/or by core–shell formation [Patra, et al, (2003), Patra, et al. (2009), Parchur, et al (2014), Yi, et al. (2006)]. Moreover, the intensity of Ln^{3+}-doped up-conversion materials strongly depends on intra 4f-4f transition probabilities and is also influenced by the crystal field symmetry and crystallinity of the samples [Dhananjaya, et al. (2011), Cheng, et al. (2012)]. Li^+ ions can be doped in the host matrices efficiently because of their small ionic radius, either by substitution or interstitial. The substitution and/or interstitial incorporation of Li^+ ions in the Ln^{3+}-doped host matrices distorts the lattice symmetry of the crystal field around the Ln^{3+} ions (Er^{3+} in our case), thus improving the up-conversion intensity [Cheng, et al. (2012), Parchur, et al. (2012b)]. Several studies have reported the improvements in up-conversion intensities for different host matrices by Li^+ ion co-doping. Chen; et al. (2008) reported 25-fold improvement in the visible up-conversion intensity in Y_2O_3:Er^{3+}/Yb^{3+}/Li^+-doped nano-phosphors, while 30-fold improvement has been obtained after Li^+ incorporation in $NaGdF_4$: Er^{3+}/Yb^{3+}host matrices (Wang et al, 2010). On the basis of more detailed studies it could be proposed that the change in crystal symmetry around the Ln^{3+} ions is one of the reasons for this luminescence enhancement [Bai, et al. (2008), Li, et al. (2012)].

One of the applications of the fluorescence measurements is estimation of temperature of the source in the conditions where the conventional method doesn't work. In recent years, fluorescence-based temperature-sensing technique has attracted much attention and seems to play a vital role because it can avoid the problem of strong signal-to-noise ratio (SNR) and hazardous sparks, which are not possible in conventional temperature sensors such as thermocouple detectors in oil refineries and coal mines [Wade, et al. (2003), Rai, et al. (2013), Brites, et al. (2011)]. The conventional temperature sensors based on the liquid and metal expansion principle, temperature is measured by the heat flow using an invasive probe. However there are situations where they cannot be used such as furnaces, jet engine, power plants etc.

The FIR technique based on the measurement of luminescence intensities from two thermally coupled levels of Ln^{3+} ions is independent of spectrum losses and fluctuations in the excitation intensity of source; therefore, it can give a more accurate temperature

measurement [Li, et al. (2014)]. One of the requirements of such devices is that the operating temperature range and sensitivity should be high for a high-quality temperature sensor. The search for a new class of material for this purpose is challenging and still underway. Fluorescence intensity ratio (FIR) of two thermally coupled levels is used in optical thermometry. FIR has been much easier and found suitable to use. This approach employs the ratio of fluorescence intensity from two excited and (normally) thermally coupled energy levels of the RE ion implanted into a suitable host [Fischer, et al. (2011)]. Fluorescence intensity ratio (FIR) has ability to cover a wide range (-196 to 1350 ^{0}C) with reasonable measurement resolution [Rai, et al. (2006), Rai, et al. (2007a and b), Dong, et al. (2008)]. The possible application of the FIR technique to measure the temperature was proposed by [Kusama, et al. (1976)] using the Boltzmann distribution law. Since then, many RE ions have been investigated not only in glasses/fibres but also in phosphor materials [Wade, et al. (1999), Wade, et al. (2003), Camrago, et al. (2006), Dong, et al. (2007)].

Herein, we report a structural, up-conversion, and temperature-sensing approach by introducing Li$^+$ ions into Y$_2$Ti$_2$O$_7$:Er^{3+}/Yb^{3+} phosphor prepared by a conventional solid-state reaction method. The structures of the phosphors with different amounts of Li$^+$ ion concentrations were analysed by X-ray diffraction (XRD), Fourier transform infrared (FTIR) spectroscopy, X-ray photoelectron spectroscopy (XPS), and field-emission scanning electron microscopy (FE-SEM). A substantial change in the up-conversion intensity and decay time (τ) of intermediate ^{4}S$_{3/2}$ (green band) state was monitored. The mechanism involved in the up-conversion process was elucidated by pump power dependence, suitable energy level diagram, and decay studies. To study the temperature-sensing behaviour, an FIR-based technique was used. To the best of our knowledge, no temperature-sensing studies have been conducted for the Er^{3+}/Yb^{3+} and Li$^+$ tri-doped Y$_2$Ti$_2$O$_7$pyrochlore system. The thermally coupled ^{2}H$_{11/2}$ and ^{4}S$_{3/2}$ levels of Er^{3+} ions in the spectrum demonstrated temperature-dependant behaviour and probed for optical thermometry using the FIR technique.

5.2   Experimental

5.1.1 Sample Preparation

Er$_x$Yb$_y$Li$_z$Y$_{2-x-y-z}$Ti$_2$O$_7$ (x=1 and y=2 at%, z = 0, 2, 5, 7, 10, and 15 at%) samples were prepared by a conventional solid-state ceramic method. Analytical reagent (AR) grade yttrium oxide (Y$_2$O$_3$, Alfa Aessar, 99.99%), titanium oxide (TiO$_2$, 99.9%, Alfa Aessar),

ytterbium oxide (Yb_2O_3, Alfa Aessar, 99.99%), erbium oxide (Er_2O_3, Alfa Aessar, 99.98%) and lithium carbonate (Li_2CO_3, Merck, 99.98%) were used as the starting materials. Stoichiometric amounts of starting materials were mixed in a planetary ball mill with zirconia jars and zirconia balls for 6 h at 50 rpm using acetone as the mixing medium (solvent). The dried mixed powders were calcined in an alumina crucible in ambient atmosphere (air) at 1200 °C for 6 h, and then the samples were furnace cooled to room temperature. A few drops of a 2% solution of polyvinyl alcohol (PVA) were added to the powder as the binder. The calcined powders were ground, mixed, and pelletized at 75 kN. The pellets were sintered at 1300 °C for 12 h. During the sintering, the pellets were initially heated at a rate of 2 °C per min to 500 °C and then kept at this temperature for 1 h to evaporate the binder. Then, the pellets were heated at a rate of 4 °C per min to the sintering temperature of 1300 °C. After sintering, the samples were furnace cooled to room temperature.

5.1.2 Characterization techniques

The structure of the phosphor was identified by XRD using a Rigaku miniflex-II diffractometer and $Cu_{K\alpha}$ radiation (1.5406 Å) at ~30 kV and 15 mA. All the patterns were recorded from $2\theta =10°$ to 90° with a step size of 0.02°. The FTIR spectra of the samples were recorded using a Shimadzu spectrophotometer in the range 4000–400 cm^{-1}. The sample was mixed with KBr (Sigma Aldrich, 99.99%) in a 1:5 ratio, and a transparent pellet was prepared. Micro- Raman spectra have been recorded under 514.5 nm Ar^+excitation at room temperature. The chemical composition and valence state of the elements were analysed by XPS using a monochromatic AlK_α (hv =1486.6eV) X-ray source and a hemispherical analyzer (SPECS, HSA3500). The recorded spectra were charge-corrected to the C1s ~284.6 eV as the reference. The morphology of the synthesised samples were examined by FE-SEM, model JEOL JSM-6700 (Japan). Osmium was coated by spraying it on the sample surfaces using a Hitachi (Japan) fine coat ion sputter E-1010 unit. To avoid the expected charging of the specimens, the coating was performed each time before the FE-SEM observation. The up-conversion emission spectra were recorded using a Princeton triple-grating turret monochromator (Acton SP-2300) equipped with a photomultiplier tube (PMT) and a personal computer (PC). The samples were irradiated using a 976 nm (CW) laser at different laser powers (i.e., 0.3 to 2.4 W) with a spot size of~1.4 mm. For the up-conversion at different temperatures, the laser beam was focused at

the edge of the pellet samples, and a thermocouple was placed close to the focal spot. Also for the study of FIR variation with laser power density, the upconversion (UC) spectra of the phosphors have been recorded at different excitation power densities at room temperature. Lifetime decay (τ) measurements were carried out by chopping the ~976 nm laser beam with a mechanical chopper and using a quick start digital oscilloscope.

5.3   Results and discussion

5.1.3 Structural Analysis

5.1.3.1 XRD Analysis

The XRD patterns of $Y_2Ti_2O_7$:Er^{3+}/Yb^{3+} (EYYTO) co-doped with Li^+ (0, 2, 5, 7, 10, and 15 at.%) ions are shown in Figure 5.1(a). All the observed intensity patterns of Li^+ co-doped samples matched well with typical face centred cubic pyrochlore (JCPDS card no. 42-0413) [Singh, et al. (2013)].The co-doping of Li^+ ions did not produce any other impurity phase in $Y_2Ti_2O_7$ (YTO) system. The expansion of main diffraction peak (222) for all Li^+(0, 2, 5, 7, 10, and 15 at.%) co-doped samples is shown in Figure 5.1(b).
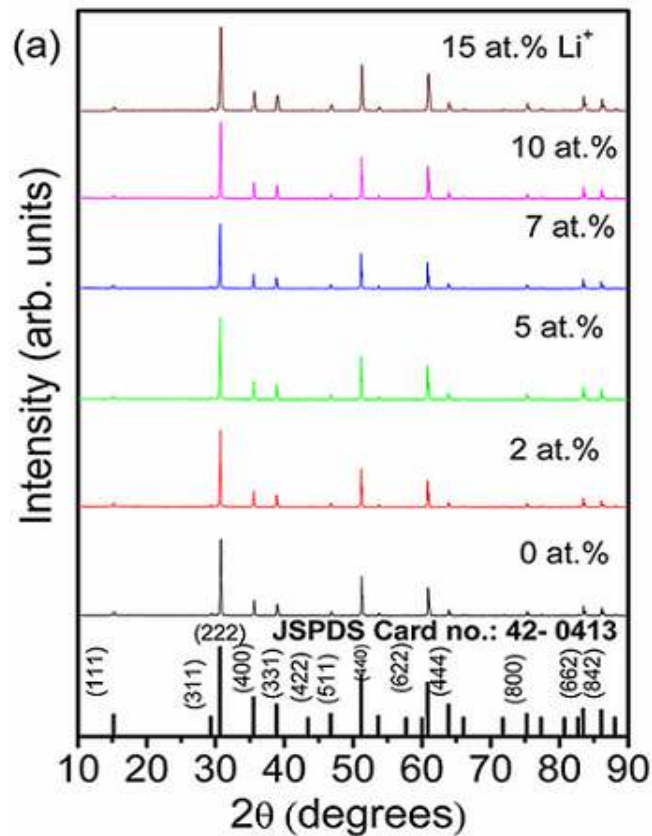

Figure 5.1: XRD pattern of (a) Er^{3+}/Yb^{3+} doped $Y_2Ti_2O_7$ and Li^+ (2, 5, 7, 10 and 15 at.%) co-doped $Y_2Ti_2O_7$
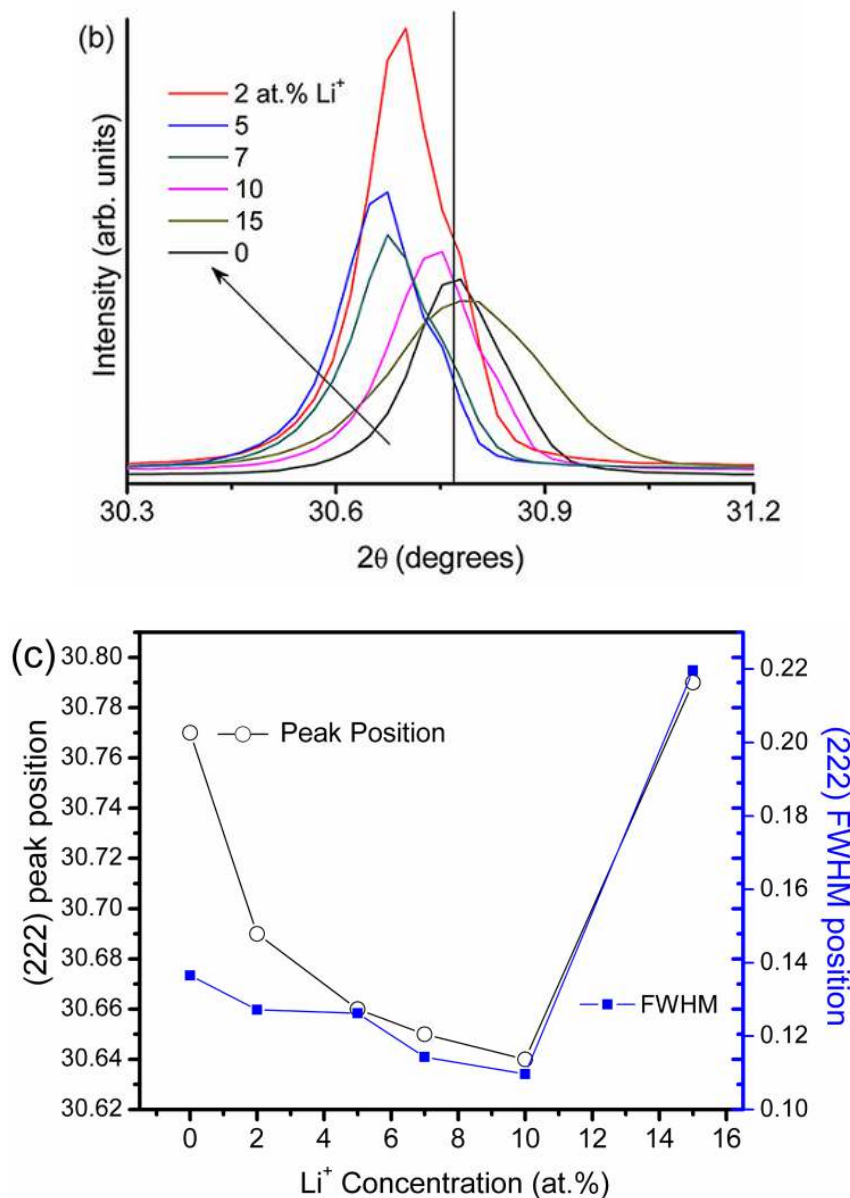
Figure 5.1: (b) Shifting of (222) peak with Li^+ ion concentration and (c) Change in peak position and FWHM of (222) peak in 2θ.

The peak position corresponding to (222) shifted to a lower angle (2θ) side up to 10 at.% Li^+, and it shifted to a higher angle side for 15 at.% Li^+. The peak position of the diffraction peak (222) and full width at half maximum (FWHM) for different Li^+ concentrations are shown in Figure 5.1(c). The shifting of main diffraction peak position indicates that Li^+ions can be occupied in both ways either via substitution or entering into interstitial sites of host matrices. Because the effective ionic radii of Li^+ , Er^{3+} , Yb^{3+}, and Y^{3+} are ~0.76, 0.89, 0.985, and 0.9Å, respectively, [Shanon, (1976)] there is a debate on Li^+ co-doped systems: on Li^+ doping, whether Li^+ ions can be substituted and/or incorporated into interstitial sites. It was reported that YPO_4:Eu unit cell volume was significantly

122

enhanced by Li^+ co-doping. Moreover, the shifting of main diffraction peaks towards lower angle side (2θ) demonstrates that Li^+ ions were incorporated into interstitial sites [Parchur, et al. (2012)]. We have not observed any other phases upto 15 at.% doped Li^+ into EYYTO samples. The intensity of diffraction patterns increased up to 2 at.% Li^+ co-doping and then decreased, indicating the association of surface defects on the surface of the samples. To understand the structural changes, Rietveld analysis was performed on the XRD data using the *FullProf* software [Rodriguez J.-Carvajal].The peak profiles were modelled using Pseudo-Voigt function and the background was described in terms of a six-coefficient polynomial. The R_{wp} (weighted-pattern factor) and S (goodness-of-fit) parameters were used as the numerical criteria for the quality of the calculated fit to the experimental diffraction data. In $Y_2Ti_2O_7$, there are four different crystallographic axes, namely, Y: (16d), Ti: (16c), O1 (48f), and O2 (8b) assuming that a Ti^{4+} ion is situated at the origin of the unit cell. The Y and Ti sites have eight and six ion co-ordination sites, respectively, while the crystallographically different axes of oxygen O1 (48f) was co-ordinated to 2Ti and 2Y. O2 (8b) was co-ordinated to 4Y ions, while the third anionic site, O3 (8a), was co-ordinated to the 4Ti ions and generally found to be empty in ordered pyrochlore lattice [Mandal, et al. (2007), Subramanian, et al. (1983)]. Since change of peak in lower 2θ upon co-doping of 10 at.%, Li^+ ions occupy interstitial sites or even grain boundary. However, we do not see Li_2O peaks. This may be due to very low atomic scattering of X-rays from Li^+ ions, which is undetectable in our XRD instrument. There will be charge balance after Li^+ co-doping in lattice and this can be compensated by introduction of oxygen vacancy or/and conversion of some Ti^{4+} ions to Ti^{3+} ions [Sala, et al. (2014)]. In this view, we analyse Rietveld plot for $Y_2T_2O_7:Er^{3+}/Yb^{3+}$ (Li = 0 at.%) (Shown in Figure 5.3). However, the detail structures for Li-codoping samples can be solved by Neutron scattering technique.

Figure 5.2 shows the Rietveld refinement of the powder diffraction data of Li^+ (0 at.%) co-doped EYYTO. The Bragg reflections and the difference in observed and calculated intensities are shown in the figure. In the crystal structure, Y and Ti occupy the special positions with *Fd3m* space group (no. 227). Y and Ti atoms occupy the same crystallographic sites (16d and 16c Wyckoff positions). Further, Y is associated with eight ion co-ordination making YO_8 polyhedral, while Ti has six ion co- ordinations by forming TiO_6 polyhedron. There are two types of oxygen atoms: O1(48f) and O2(8b).
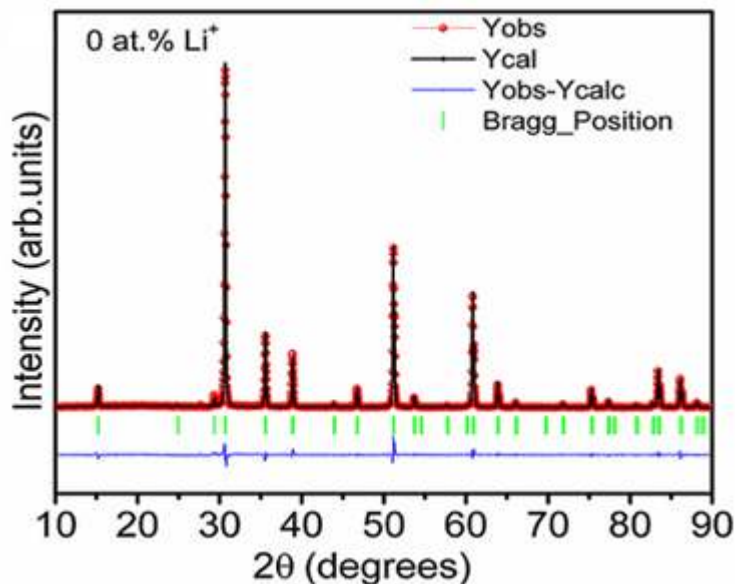
Figure 5.2: Observed, calculated, and difference X-ray diffraction patterns of Li^+ (0 at.%)co-doped $Er^{3+}/Yb^{3+}:Y_2Ti_2O_7$

The refined parameters e.g., atoms/ions, Wyckoff positions, thermal parameters, and site occupancy and lattice parameters for Li^+ free $Y_2T_2O_7:Er^{3+}/Yb^{3+}$ sample is listed in Table5.1.

Table 5.1: Atomic Coordinates, Isotropic Thermal Parameters, and Occupancy Obtained from Rietveld Refinement.

Samples $Y_2Ti_2O_7:Er^{3+}/Yb^{3+}$	Atom	Site	x	y	z	U ($Å^2$)	Occupancy
	Y	16d	0.5	0.5	0.5	0.011	1.97
	Er	16d	0.5	0.5	0.5	0.011	0.01
	Yb	16d	0.5	0.5	0.5	0.011	0.02
$0Li^+$	Ti	16c	0	0	0	0.009	2.00
	O1	48f	0.324(5)	0.125	0.125	0.002	6.00
	O2	8b	0.375	0.375	0.375	0.005	0.97

a= 10.095(1) Å, V = 1028.64(3), R_{wp}=13.4, R_p=15.7, χ^2 = 4.2

There are two types of bond involvement in YO_8 group, (Y–O1) and (Y–O2), while the TiO_6 group showed only one type of bond (Ti-O1).The bond lengths of Y–O1 was found 2.512 Å, whereas the bond length of Y–O2 was ~2.185 Å for Li^+ free sample. Selected bond distances and co-ordination numbers of Li^+ free $Y_2Ti_2O_7$:Er^{3+}/Yb^{3+} obtained from the Rietveld refinement are listed in Table 5.2.

Table 5.2: Selected Bond Distances Obtained from Rietveld Refinement.

Samples $Y_2Ti_2O_7$:Er^{3+}/Yb^{3+}	Bond Type	CN	Bond Length(Å)
	Y(16d)-O1(48f)	6	2.5124(2)
0Li^+	Y(16d)-O2(8b)	2	2.1855(3)
	Ti(16c)-O1(48f)	6	1.9377(6)

5.1.3.2 XPS Study

To investigate the chemical composition of material surface, X-ray photon spectroscopy (XPS) technique was used. The XPS data of elements thus obtained were charge corrected with respect to C 1s, which appeared at ~284.6 eV; it arises mainly because of the presence of adventitious carbon during atmospheric exposure. The survey scan of core binding energy (BE) of Y, Ti, O, Er, Yb, and Li in the range 0–1100 eV and XPS spectra showing the core BE and intensity of Er(4d), Yb(4d), and Li(1s) with Li^+ concentration are shown in Figure 5.3 (a)-(d) ;their profile peaks matched well with those reported in literature [Huang, et al. (2013), Jia, et al. (2010), Saha, et al. (2013)]. Because of the lower concentration of Er^{3+}, Yb^{3+}, and Li^+ present in the sample, a comparatively low intensity was observed.
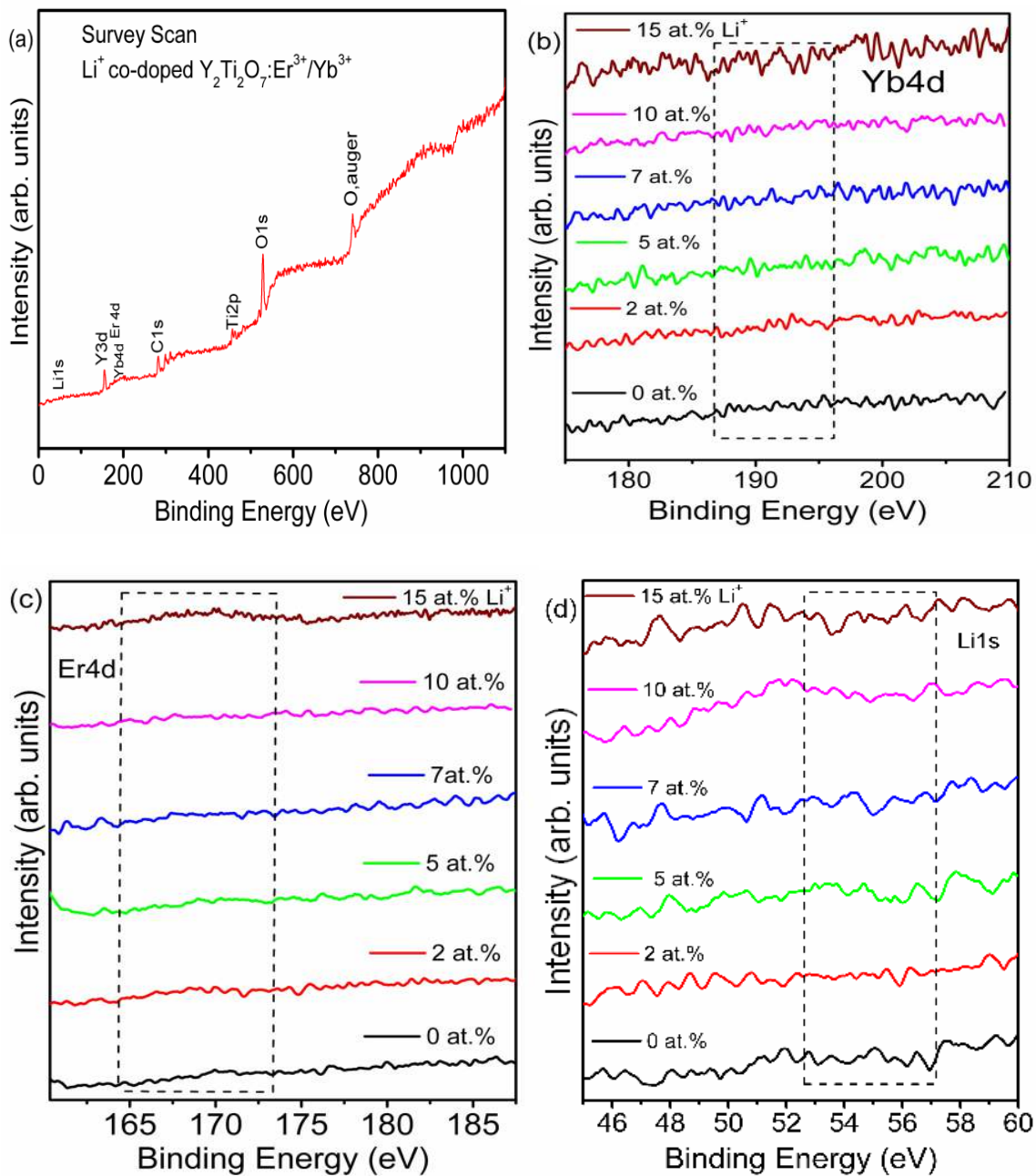
Figure 5.3: (a) Survey Scan of 2 at.% Li^+ co-doped $Y_2Ti_2O_7$:Er^{3+}/Yb^{3+} (b) XPS spectra of Yb(4d), (c) XPS spectra of Er(4d) and (d) XPS spectra of Li1s.

Figure 5.4(a) (i)–(vi) show the XPS spectra of Y (3d) for 0, 2, 5, 7, 10, and 15 at% Li^+ co-doped EYYTO samples obtained in the range 153–162 eV. For Li^+-free EYYTO samples, the peak corresponding to Y(3d) had a core BE of ~156.85 eV (3$d_{5/2}$) and 158.92 eV (3$d_{3/2}$) and a FWHM of ~2.2 and 2.3 eV. On increasing Li^+(2, 5, 7, 10, and 15 at%)co-doping concentration, there was a slight change in BE (±0.63 eV) and FWHM (±0.3 eV) corresponding to Y3$d_{5/2}$ peak towards higher energy within the limits of error bar.

126

Moreover, a very nominal change in BE (±0.59 eV) and FWHM (±0.5 eV) corresponding to $Y3d_{3/2}$ peak was observed. These results confirm the +3 formal oxidation state of Y [Parchur, et al. (2012)]. Moreover, the integrated intensity ratio of $(3d_{5/2})$ to $(3d_{3/2})$ was found to be~1.64, 2.89, 1.54, 0.85, 1.79, and ~1.74 for 0, 2, 5, 7, 10, and 15 at.% Li^+ co-doping, respectively.
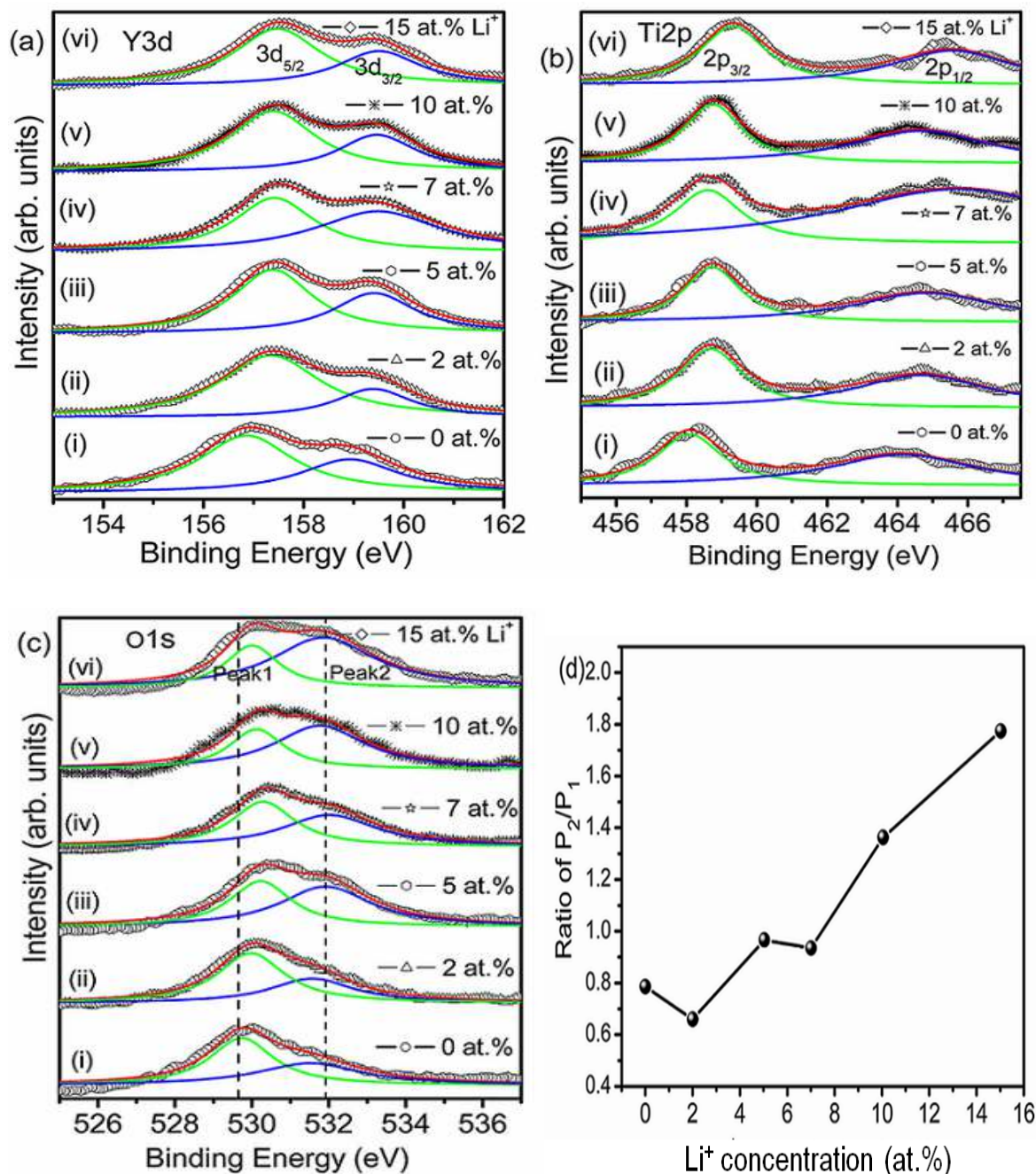

Figure 5.4: XPS spectra of (a) Y (3d) (b) Ti (2p) and (c) O (1s) of Li^+ co-doped $Y_2Ti_2O_7$:Er^{3+}/Yb^{3+} (at.% of Li^+ ion is shown in figure itself) and (d) ratio of deconvoluted relative peak positions with respect to Li^+ ion concentration.

The XPS spectra of the core BE of $Ti2p_{3/2}$ and $Ti2p_{1/2}$ regions (between 455–467 eV) are shown in Figure 5.4(b) (i)–(vi). It has been reported in literature that Ti in its +4 oxidation state has BE values in the range ~458–460 eV for $2p_{3/2}$level [Huang, et al. (2013)]. Notably, diverse BE has been reported for Ti^{4+} ions. Hence, the energy separation between the O1s and BE of $Ti(2p_{3/2})$ was investigated. Hence, the energy separation between the O1s and BE of $Ti(2p_{3/2})$ was investigated to determine the valence state of Ti ions. The energy separation, i.e., $(O1s-2p_{3/2})$, was found to be in the range 71.3 ± 0.35 eV, demonstrating +4 oxidation state in EYYTO sample. Christopher and Swamy, (1991) reported the XPS study of titanates; the peak at ~464.1 eV was attributed to the core BE of Ti $(2p_{1/2})$. Moreover, they also mentioned some satellite peaks at 462.2 and 469.7 eV for $2p_{3/2}$and $2p_{1/2}$levels, respectively. The XPS spectra of O1s are used as a probe for investigating the presence of oxygen ion vacancies on the surface of a sample. The peaks were de-convoluted using Lorentzian function. In the case of Li^+-free EYYTO sample, the two peaks well fitted to BE ~529.7 (P_1) and 531.5 eV (P_2) with FWHM ~1.8 and 3.2 eV, respectively. On increasing Li^+ co-doping, the peak position slightly changed from $\pm$ 0.08 to 0.5 eV (Figure 5.4(c)). On Li^+ co-doping, all the peaks showed asymmetric behaviour towards higher BE. Moreover, the two peaks, further attributed to the presence of two non-equivalent crystallographic sites, were present in the typical pyrochlore system $(A_2B_2O_6O')$. Further, the relative area of the P_2/P_1 ratio of Li^+(0, 2, 5, 7, 10, and 15 at%) EYYTO samples provided an interesting feature, as shown in Figure 5.4(d). The ratio of P_2/P_1 decreased for 2 at.% Li^+ compared to Li^+-free sample, and it shows an increasing trend for higher at.% of Li^+ concentration. This is probably because of the creation of oxygen ion vacancies and/or surface defects through the sample surface with the introduction of Li^+ ions into the host matrix [Saha, et al. (2013)]

5.1.3.3 FTIR Studies

Figure 5.5 (a-f) show the FT-IR spectra of Li^+(0, 2, 5, 7, 10, and 15 at%) co-doped $Y_2Ti_2O_7{:}Er^{3+}/Yb^{3+}$. The phonon cut-off energy bands at 417 cm^{-1} (Y–O1), 463 cm^{-1}(Y–O2), and at 573 cm^{-1} (Ti–O1) were almost identical for all the samples, dictating the lattice vibrational mode; thus, the multi-phonon non-radiative decay channel was not altered by further doping of Li^+ ions. Moreover, the formation of pure phase $Y_2Ti_2O_7{:}Er^{3+}/Yb^{3+}$ and Li^+ (2, 5, 7, 10, and 15 at%) co-doped $Y_2Ti_2O_7{:}Er^{3+}/Yb^{3+}$ phosphors was supported by FTIR analysis [Singh, et al. (2013)].
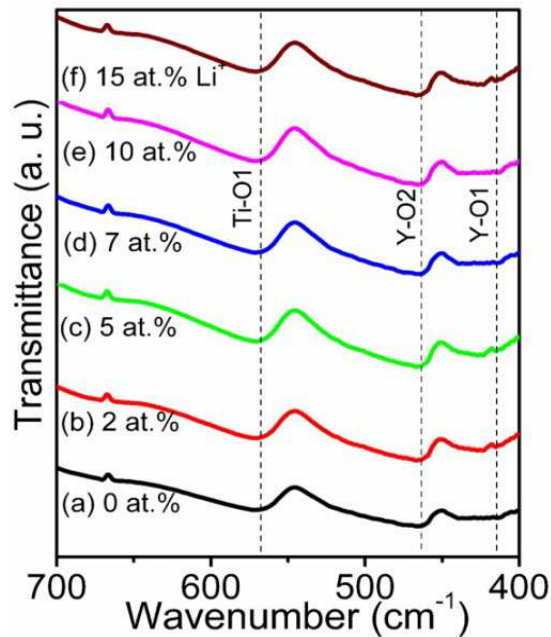
Figure 5.5: Measured FT-IR transmission spectra of $Y_2Ti_2O_7$:Yb^{3+}/Er^{3+}/Li^+ co-doped phosphors: (a) 0 at.%, (b) 2 at.% , (c) 5 at.%%, (d) 7 at.% , (e) 10 at.% and (f) 15 at.% Li^+ ion.

5.1.3.4 Raman Analysis

Figure 5.6 shows the Raman spectra of Li^+ (0, 2, 5, 7, 10, and 15 at%) co-doped $Y_2Ti_2O_7$. Raman technique is more sensitive to metal-oxygen vibrational modes and hence probed for the local disorder present in the lattice. Because pyrochlore can be seen as a superstructure of fluorite induced by the ordering of A and B cations into nonequivalent crystallographic sites and the ordering of anions into three sites *48f, 8a*, and *8b* the latter remaining empty in a perfectly ordered lattice, a brief description of pyrochlore and fluorite Raman activity is relevant. In a perfect AO_2 fluorite (*Fm3m* space group, $Z = 4$), only one mode (T_{2g}) is expected, which involves oxygen vibration in the tetrahedral cage formed by four A cations. In $A_2B_2O_7$ pyrochlores (*Fd3m*, $Z = 8$) there are six Raman active modes (A_{1g}, E_g, $4T_{2g}$), involving only vibrations of oxygens at both 48f and 8a sites [Sanju´an, et al. (2011)]. According to group theory irreducible representation Raman spectra revealing pyrochlore structures having six Raman active modes represented as $\Gamma = A_{1g} + E_g + E_{2g}$, where symbols represent irreducible group representation. The active Raman bands were A_{1g}, E_g and $4T_{2g}$ while IR active is 7F1u [Brown, et al. (2003)]. Sanjuan*, et al.* (2011) explained the characteristic modes of YTO pyrochlore observed at 310 cm^{-1} which has the contributions from E_g and T_{2g} modes both. The bands at 515 and 711 cm^{-1} correspond to A_{1g} mode of vibration in the Raman spectra occurs (Shown in Figure 5.7). The A_{1g} fre-

quency mode provides information about the force constant of the $Y_2Ti_2O_7$ pyrochlore. The vibration of the $TiO6$ octahedron is responsible for the $A1g$ mode of vibration of $Y_2Ti_2O_7$ pyrochlore structure. The major contribution for this mode is mainly due to force constants associated with O–Ti–O bending [Sanjuán, et al. (2011)]. Recently, Camacho, et al. (2013) studied the Raman spectra of Er^{3+}/Yb^{3+} doped hybrid materials and reported that the band situated near $368cm-1$ is the metal oxygen (Yb–O) similar to the band at 377 (here $381cm^{-1}$) of (Y–O) stretching vibration, while characteristic peaks of Er–O are found in the range of 500–580 cm^{-1} and also some small traces of Raman bands near $620–680cm^{-1}$ and $780–900$ cm^{-1} are observed. Vibrational modes observed are most pronounced for 2 at% of Li^{+} indicating the best crystallinity and hence the best atomic ordering. It is worthwhile to mention that after Li^{+} co-doping, a slight broadening at 310 cm^{-1} in the Raman spectra occurs (shown in Figure 5.6). Notably, pyrochlore structure bands have been observed for Li^{+} doped EYYTO samples. It also rules out the phase segregation/change from YTO matrices.
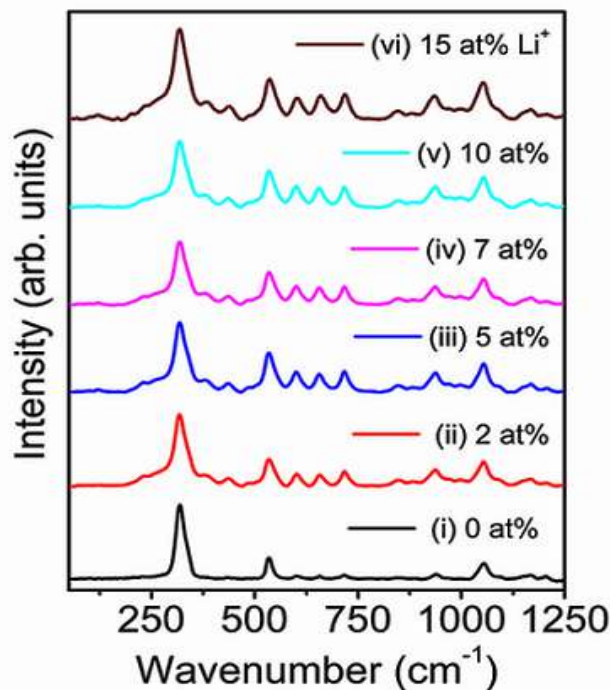

Figure 5.6: Raman spectra of Li^{+}(0, 2, 5, 7, 10 and 15 at.%) co-doped EYYTO.

Some additional weak intensity Raman bands have also been observed. These are bands related the vacancies, defects, and foreign ions in the ordered lattice which disrupts the translational symmetry (i.e. k = 0 selection rule is relaxed). Phonons having all parts of the Brillouin zone contributed to the optical spectra, thereby resulting in broad bands.

Tyagi, et al. (2011) have reported the Dy^{3+} substituted $Sm_2Zr_2O_7$ and observed the broadening in the Raman spectra on the Dy^{3+} substitution. Even a very broad peak was observed upon heavy doping of Dy^{3+}. However we do not observe such broadening even upon doping of 15 at% Li^+. Still peaks corresponding Raman bands are sharp. It means that Li^+ ions do affect pyrochlore structure. Most Li^+ ions occupy either interstitial sites or grain boundary, which is predicted by XRD study. Even, if Li_2O is present in particles, it should be seen in Raman spectra. Pure Li_2O crystallizes in the anti-fluoride structure and it gives only one allowed Raman band at 523 cm^{-1} [Osaka and Shinde(1984)]. This peak is merged with the allowed transition of Raman band of $Y_2Ti_2O_7$ pyrochlore. Thus, we could not distinguish the presence of Li_2O compound even if it is present.

Moreover for the completely ordered pyrochlore ($A_2B_2O_7$), phase stability of the superstructure is predominantly determined by cationic radius ratio of the site A and B. It has been well documented in the literature that the pyrochlore lattice is supported by a radius ratio, r_A/r_B. The value of cationic radius ratio varies between 1.46 and 1.78 for ordered pyrochlore structure [Tyagi, et al. (2011)].

5.1.3.5 SEM Studies

Figure 5.7(a) shows the FESEM image of $Y_2Ti_2O_7$:Er^{3+}/Yb^{3+}, (Figures. 5.7(b)–(f)) represent the morphology of Li^+ (2, 5, 7, 10, and 15 at.%) co-doped EYYTO. Prominent modification of the microstructure was observed from the micrographs of the Li^+ co-doped samples. Li^+-free EYYTO sample corroborates an inhomogeneous uneven morphology. As far as Li^+ co-doped EYYTO samples is concerned, 2 at.% of Li^+ sample showed the highest roughness than the samples with higher concentrations of Li^+. This indicates that the absorption of incident photons increases with increasing roughness of the sample; thus, the highest emission intensity is observed. Fan, et al.(2011) and Sun, et al.(2001) also proposed that the increased roughness and crystallinity of materials, in the presence of Li^+ doping, are among one of the significant reasons for the enhancement in the luminescence intensity of lanthanides. However, a further incorporation of Li^+ ions in the sample reduced the crystallinity, and the morphology became irregular (as shown in Figsures 5.7(c)–(f)) with the defects induced on the sample surface. The micro-structural properties of the samples play a vital role for PL characteristics, because of the better crystallinity of the host–activator system transferring energy efficiently from the host to the activator, which was further confirmed by the respective PL spectra.
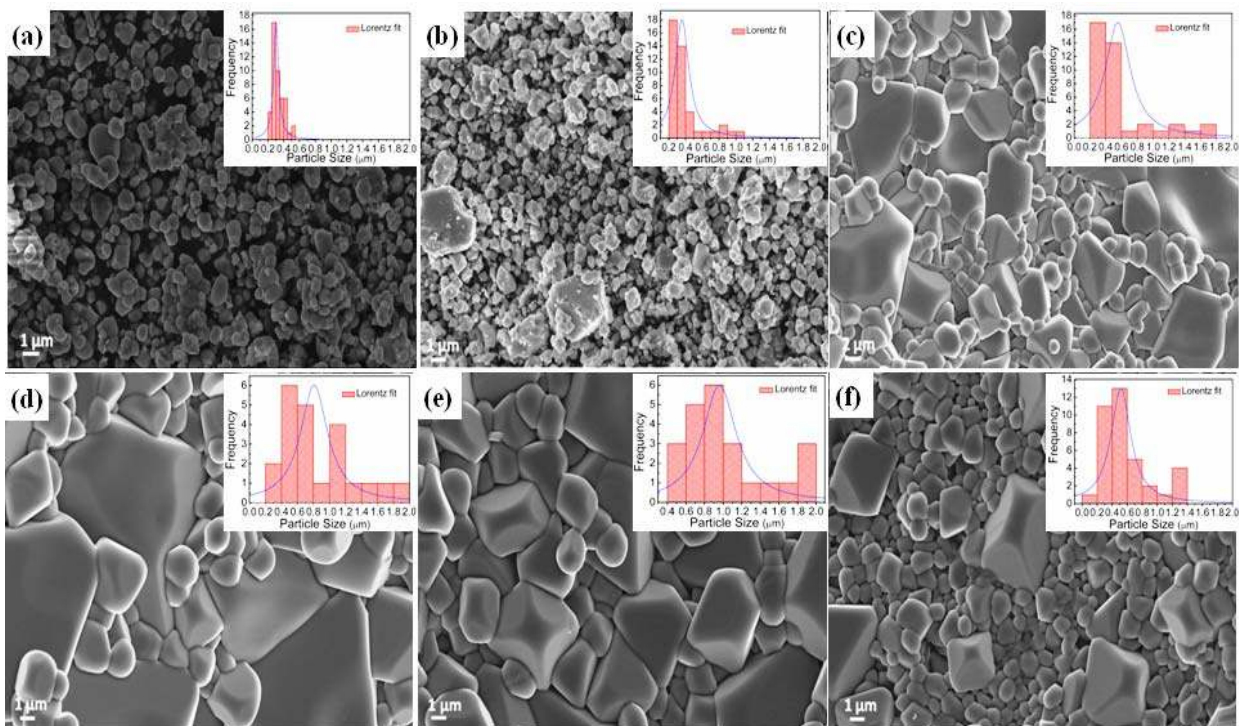
Figure 5.7: FE- SEM micrographs of Li^+ co-doped $Y_2Ti_2O_7$: Er^{3+}/Yb^{3+} (a) Li^+free (b) 2 at.%(c) 5 at.% (d)7 at.% (e) 10 at.% and (f) 15 at.% Li^+.

Particles exhibit an irregular morphology because of the inherent characteristics of the used solid-state reaction method. Figures 5.7(c), (d), (e), and (f) show that the particles almost have polyhedron morphology. From the SEM micrographs, it is evident that the particle size evolution is in the order of micron. For 15 at% co-doped sample, more uniform spherical microspheres of average diameter in the range ~0.5–1.5 µm than rough cube-like structures were observed. Infact, the percentage of rough cube-like structures first increased with Li^+ co-doping up to 10 at% and then decreased. This is also supported by the XRD peak broadening (Figure 5.1(b)). The histograms of the average particle size distribution of the particles are shown in the figures.

5.4   Optical Studies

5.1.4   Upconversion Studies

The up-conversion properties of Li^+(0, 2, 5, 7, 10, and 15 at%) co-doped EYYTO have been studied at room temperature under ~976 nm excitation. The variation in up-conversion emission intensity *versus* Li^+ concentration is shown in Figure 5.8.The up-conversion intensities show brilliant green emission followed by red emission. Two prominent bands were observed because of the up-conversion at ~524 and 548 nm, which

are responsible for the green emission in the range 500–600 nm with the maximum intensity at ~548 nm. These two bands can be attributed to the $^2H_{11/2} \rightarrow ^4I_{15/2}$ and $^4S_{3/2} \rightarrow ^4I_{15/2}$ electronic transitions of Er^{3+} ion, respectively. Moreover, the band observed in the range 600–700 nm with the maximum intensity at ~661nm was assigned to the $^4F_{9/2} \rightarrow ^4I_{15/2}$ transition of Er^{3+}. Moreover, the peaks at ~380, 410, and 487 nm in the near-UV and blue regions of the spectrum with a low intensity is well described in the inset of Figure 5.8(a) (i) in the range 380–500 nm. These bands can be attributed to the electronic transitions, namely, the $^4G_{11/2} \rightarrow ^4I_{15/2}$, $^2H_{9/2} \rightarrow ^4I_{15/2}$, and $^4F_{5/2} \rightarrow ^4I_{15/2}$ of Er^{3+} ion on 976 nm excitation.
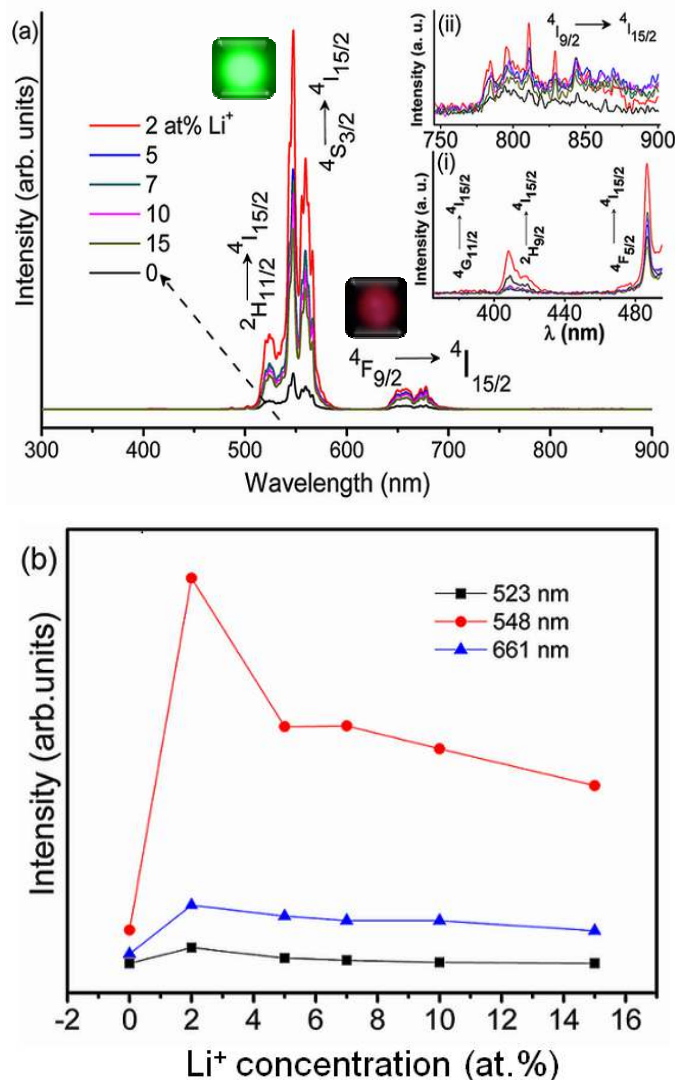

Figure 5.8: (a) Emission spectra of Li^+ (0, 2, 5, 7, 10, and 15 at%) co-doped $Y_2Ti_2O_7$:Er^{3+}/Yb^{3+} phosphor under 976 nm excitation. Insets (i) and (ii) show the expansion in 380–500 nm and 750–900 nm. The digital photographs of EYYTO:2Li$^+$ were recorded using a Nikon Coolpix P500 digital camera using a suitable colour filters and (b) shows the integral intensity of green and red emissions as a function of the concentration of Li^+ ions.

133

The inset (ii) of Figure 5.8(a) in the range 750–900 nm, with a well-splitted Stark pattern of the $^4I_{9/2} \to {}^4I_{15/2}$ transition of Er^{3+} ion, demonstrating the highly crystalline nature of EYYTO phosphor [Singh, et al. (2013)].The variation in up-conversion intensity was observed with Li^+ concentration and found to be the maximum for 2 at% Li^+ (as shown in Figure 5.8(a)). This is probably because the 2 at% Li^+-doped EYYTO sample has the most asymmetric environment around Er^{3+} ion. For higher concentrations of Li^+ (5, 7, 10, and 15 at%), the intensity decreased. This is because of a lower proportion of Li^+ incorporation in host lattice, thus inducing a fast ET from the host to the Er^{3+} ion. This may create the vacancies that act as the sensitizer, mixing the charge-transfer states. Li^+ addition increased the PL intensity by increasing the radiative transition probability. However, an increase in the Li^+ concentration over a certain limit generates a significant amount of oxygen ion vacancies in the lattice. Consequently, the crystal lattice collapses, and the luminescence intensity decreases [Jia, et al. (2010)]. The inset shows the digital photographs of the up-conversion luminescence of EYYTO:2Li under 976 nm excitation using a suitable filter. The fluorescence intensities of the green and red bands were measured, and enhancements of ~15 and 8 fold were observed for EYYTO:2Li, more than that of Li^+ free EYYTO sample. The integral intensities of 524, 548, and 661 nm bands showed similar trends as Li^+ concentrations, corroborating the same up-conversion pathways (Figure 5.8 (b). Clearly, the green and red up-converted emission intensities enhanced drastically with Li^+ concentration. The incorporation of Li^+ ions in both ways, substitution and/or interstitial sites changed the crystal field and surrounding environment of Er^{3+} ions. It was also confirmed by the Rietveld refinement XRD studies of all the measured samples with Li^+ concentrations. Moreover, Li^+ incorporation may change the electron density.

This change in environment around Er^{3+} may provide hypersensitive transitions with the selection rule as follows: $|\Delta J| = 2$, $|\Delta L| \nleq 2$, and $|\Delta S|=0$, increasing the population density in the $^4S_{3/2}$ state and opposing the cross-relaxation and energy back transfer; thus, different folds of enhancement were observed for the green and red up-converted bands [Cheng, et al. (2012)]. The enhanced up-conversion intensity indicates that the incorporation of different concentrations of Li^+ ions can modify the local symmetry around Er^{3+} ions; a further enhancement in Li^+ concentration decreased the up-conversion intensity. Li^+ ions with smaller ionic radii can readily occupy and/or enter into the interstitial sites of the host by lowering the crystal field symmetry around Er^{3+} ions.

Moreover, the incorporation of Li^+ ions into host would create some defects, and oxygen ion vacancies associated with sample surfaces were also confirmed by the XPS study. The oxygen ion vacancies acted as the sensitizer for Ln^{3+} ions because of the overlapping of charge-transfer states; thus, enhanced PL was observed [Lopez, et al. (1997)]. Moreover, Li^+ incorporation may also improve the system crystallinity, lower the surface defects and non-radiative transitions; thus, an enhancement in up-conversion emission intensity was observed. To determine the number of up-converted photons involved in the up-conversion process, the up-conversion luminescence intensity of $2Li^+$ co-doped EYYTO was measured as a function of pump power. The number of photons required for an unsaturated up-conversion process to populate the upper emitting levels can be well described as follows [Pollnau, et al. (2000)]:

$$I_{up} \propto I_{NIR}^n \tag{5.1}$$

where I_{up} is the up-conversion emission intensity, I_{NIR} is the pump laser intensity, and n is the number of pump photons required for up-conversion process.

The power dependence study of EYYTO:2Li sample for green and red bands is shown in Figure 5.9. The slopes (n values) obtained from the linear fitting of the bi-log plots for ~524, 548, and 661 nm were ~1.67, 1.97, and 1.61, respectively, with slightly smaller values than the Li^+-free EYYTO sample. The values of slope confirmed that two-photon processes were involved in the observed green and red emissions for both the Li^+-doped and Li^+-free samples. Moreover, the power dependence was studied for the weak UV and blue bands, i.e., for ~380, 410, and 487 nm bands, and the slope values were found to be ~2.65, 2.72, and 2.89, i.e., three-photon processes were involved in these bands, as shown in Figure 5.10. Because Li^+ ions cannot absorb ~976 nm pump photon energy, ultimately, they are unable to transfer energy to Er^{3+} ion, which further confirms that the mechanism of the up-conversion was not affected by the incorporation of Li^+ ions. Moreover, the slope values were altered slightly with Li^+ ions, with smaller values for green and red emission bands than Er^{3+}/Yb^{3+}-doped $Y_2Ti_2O_7$ bands [Singh, et al. (2013), Cheng, et al. (2012)]. Smaller n values demonstrated that the involved up-conversion process occurs comparatively easily to saturate Li^+ co-doped EYYTO than the Li^+-free EYYTO samples. Moreover, EYYTO:2Li sample emitted green light at a low excitation power density of~135 mWmm^{-2}than Li^+ free EYYTO sample with an excitation power
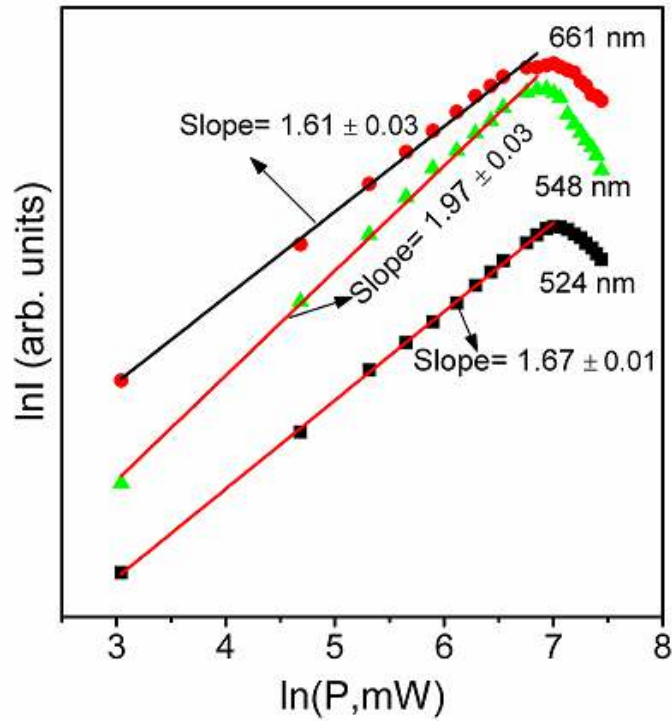
density of~152 mWmm^{-2}.

Figure 5.9: Power dependence of green and red bands (524, 548 and 661 nm).
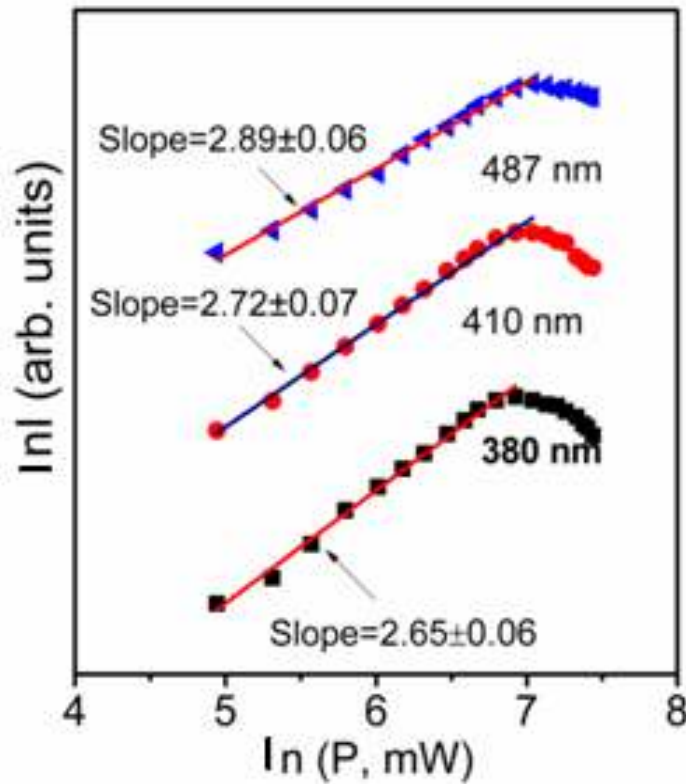

Figure 5.10: Power dependence of UV and blue bands (380, 410 and 487 nm).

Cheetham and co-workers reported the excitation power densities for (Yb^{3+}, Er^{3+}, and Tm^{3+}) and (Er^{3+} and Yb^{3+}) doped Y_2BaZnO_5 with the minimum excitation power of 25 mW mm^{-2} and 90 mW mm^{-2}, respectively [Cheetam, et al. (2011)].

5.2.1.1 Energy level diagram and energy transfer

On ~976 nm laser excitation, Er^{3+} and Yb^{3+} ions are promoted to their resonant excited states though ground-state absorption (GSA). Because Er^{3+} ions have a low absorption cross section, the GSA process was found to be weak for Er^{3+}. Yb^{3+} ions exhibit a nearly seven times higher absorption cross section (~11.7×10^{-21} cm^2) than that of their Er^{3+} counterpart (~1.7×10^{-21} cm^2) [Strohhofer and Polman (2003)]. Thus, most of the impinging photon energy was absorbed by the Yb^{3+} ions and further transferred to Er^{3+} ions *via* different (ET) processes. The details of the different ET processes for theEYYTO:2Li system are shown in Figure 5.11.
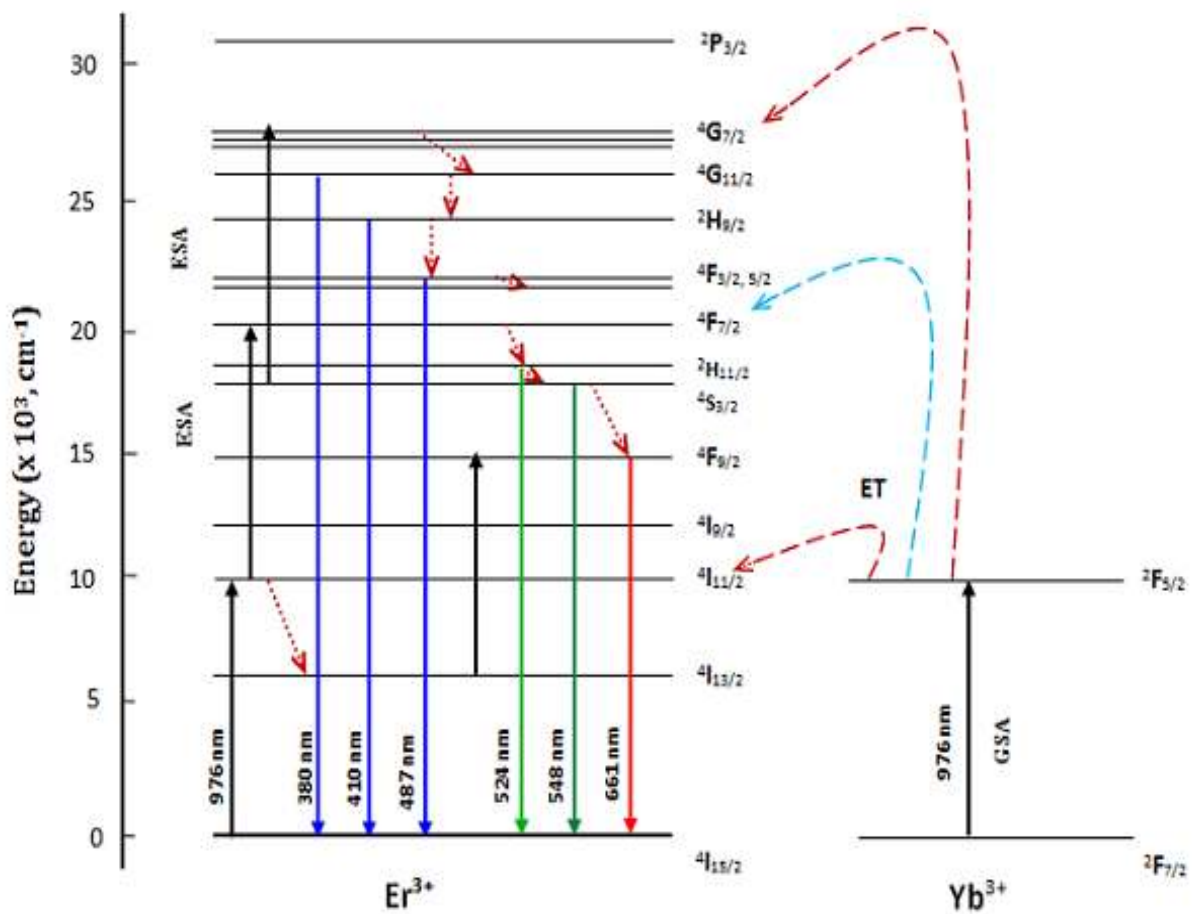

Figure 5.11: Schematic partial energy level diagram and energy transfer processes involved in the up-conversion process.

5.2.1.2 Effect of temperature on the up-conversion emission and temperature-sensing behaviour

To investigate the temperature-sensing behaviour of these phosphor (EYYTO:2Li) materials, the FIR technique was employed. In this technique, the fluorescence emitted from the thermally coupled closely spaced levels to a common final ground state is monitored, and the ratio of the emission intensities of these two bands is calculated as a function of temperature. In the case of Er^{3+}ions, the two levels, $^{2}H_{11/2}$ and $^{4}S_{3/2}$, are closely spaced ($\sim$500–600 cm^{-1}) and thermally coupled.
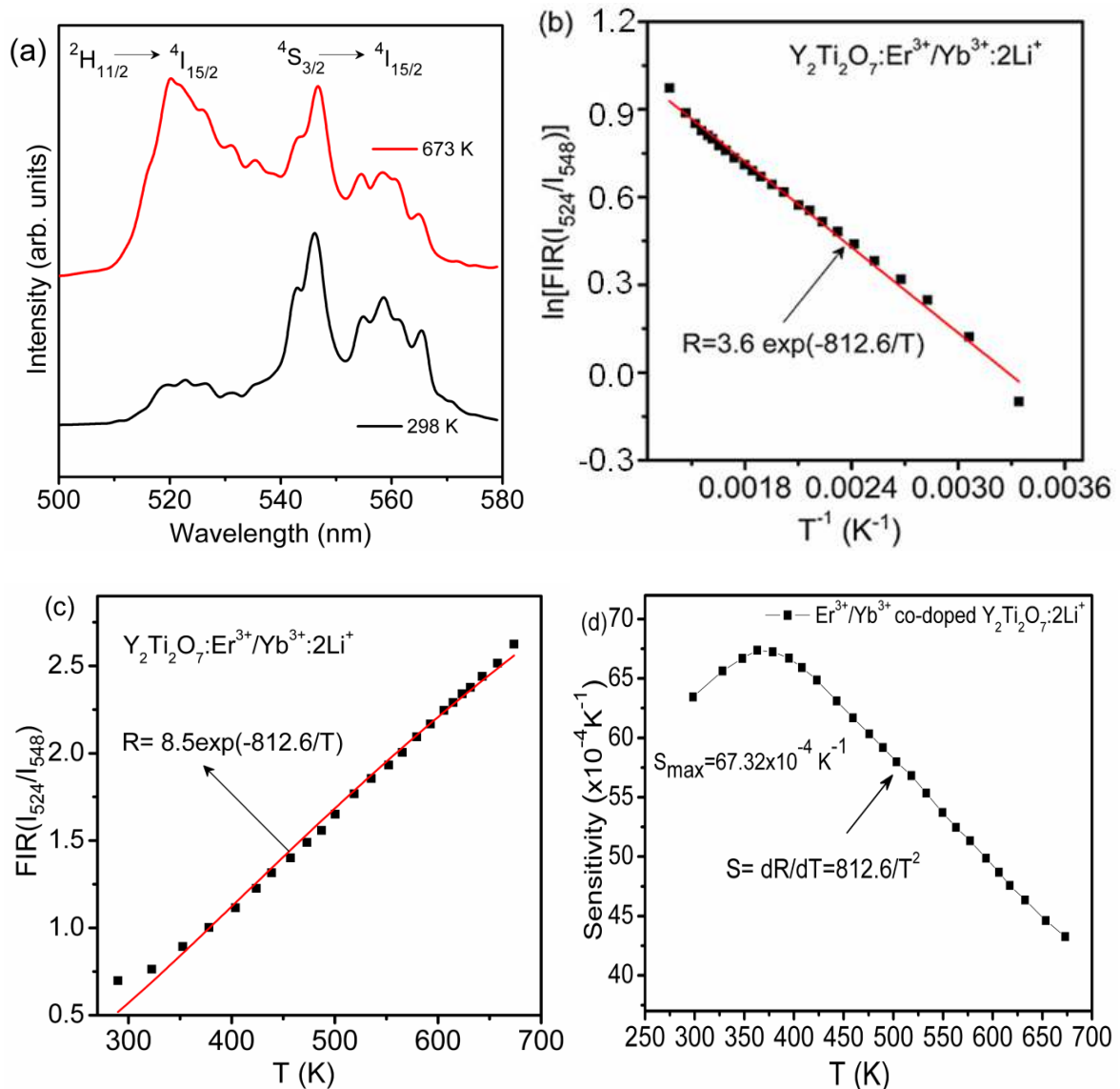
Figure 5.12: Upconversion-based temperature sensing behaviour of 2 at.% Li^{+} co-doped $Y_2Ti_2O_7$:Er^{3+}/Yb^{3+} phosphor, (a) green UC emission spectra measured at 298 and 673K, (b) monolog plot of the FIR (using 524 and548 nm emission)as a function of the inverse absolute temperature, (c) the FIR relative to the temperature and (d) sensor sensitivity as a function of the temperature.

The FIR of $^2H_{11/2}$ and $^4S_{3/2}$ levels to the ground state (i.e., $^4I_{15/2}$) of Er^{3+} level was applied to study the temperature-sensing behaviour in the temperature range 298–673 K at an excitation power of ~250 mW. Figure 5.12(a) shows the green up- conversion spectra of $2Li^+$ co-doped EYYTO in the wavelength range 510–580 nm at the measured temperatures of 298 and 673 K. The peak positions of the green up-conversion bands ($^2H_{11/2}$ and $^4S_{3/2}$ levels) did not change; however, the corresponding intensities of these two bands centred at 524 nm and 548 nm varied substantially with the increase in the sample temperature. The fluorescence intensity of the green band centred at 524 nm ($^2H_{11/2}$) is very low compared to the band centred at 548 nm at room temperature (298 K), while at the elevated temperature (673 K), the reverse trend was observed. Thus, the variation in the fluorescence intensity of the two peaks was estimated. According to Maxwell Boltzmann distribution, the photon population density of ions in the two thermally populated levels of Er^{3+}, i.e., for $^2H_{11/2}$ and $^4S_{3/2}$ can be expressed as follows: [Brites, et al. (2011); Fischer, et al. (2011)]

$$\frac{n_H}{n_S} = \frac{g_H}{g_S} \exp\left(\frac{-\Delta E}{kT}\right)$$

$$= \frac{g_H}{g_S} \exp\left(\frac{-\Delta E}{kT}\right) \tag{5.2}$$

where n_H, n_S, g_H and g_S are the corresponding particle densities and degeneracy factors associated with the levels, $^2H_{11/2}$ and $^4S_{3/2}$, respectively. ΔE is the energy gap between the two levels, k is the Boltzmann constant, and T is the absolute temperature. In general, the energy associated with $^2H_{11/2}$ level is higher than that associated with $^4S_{3/2}$ level, i.e., particle density n_H is lower than n_S, thus, the transition intensity of $^2H_{11/2} \rightarrow ^4I_{15/2}$ is weaker than that of $^4S_{3/2} \rightarrow ^4I_{15/2}$ at 298 K, as shown in Figure 5.12(a). For high temperature, the energy separation of these two levels requires the $^2H_{11/2}$ level to be populated by thermal agitation, which in turn provides a higher transition intensity of $^2H_{11/2} \rightarrow ^4I_{15/2}$ than $^4S_{3/2} \rightarrow ^4I_{15/2}$. The overall intensity of green band decreases as the sample temperature increases. This is probably because of an enhanced lattice vibration followed by non-radiative decay channel rates. The temperature-dependent up-converted green emission can be attributed to the highly stable spectra in the measured temperature range, i.e., 673 K. Thus, it has great potential in display devices. The relative population density of two thermally populated $^2H_{11/2} \rightarrow ^4I_{15/2}$ and $^4S_{3/2} \rightarrow ^4I_{15/2}$ levels follow the Maxwell

Boltzmann distribution, which led to the variation in these two thermally populated levels of fluorescence intensity.

The variation in the FIR of thermally coupled and closely spaced up-conversion bands can be expressed as: [Wade et al. (2003), Rai, et al. (2006), Wei et al. (2010)].

$$R = \frac{I_H}{I_S} = \frac{n_H}{n_S} = \frac{g_H \omega_H \sigma_H}{g_S \omega_S \sigma_S} \exp\left(\frac{-\Delta E}{kT}\right) \tag{5.3}$$

where I_H, I_S, ω_H, ω_S, σ_H and σ_S are the corresponding intensities, transition frequencies of the associated levels, and the absorption probability rates of $^2H_{11/2}$ and $^4S_{3/2}$ levels to the $^4I_{15/2}$ level, respectively, while n_h, n_s, g_h, and g_s are defined as in equation (5.2).

$$R = B \exp\left(\frac{-\Delta E}{kT}\right) \tag{5.4}$$

where B is the pre-exponential factor and ΔE, k, and T have the same meaning as defined in equation (5.2). From the above equation (5.4), it is clear that the FIR is independent of source intensity, which is the prerequisite of any temperature measuring sensing device. The variation in FIR to the relative bands centred at 524 and 548 nm as a function of inverse absolute temperature on a monolog scale is shown in Figure 5.12(b). The linear dependency of the curve demonstrates the suitability of the material in temperature-sensing applications.

The fitted slope value obtained by fitting the straight line equation gives ~812 ± 6.24 for the curve shown in the figure. The B value obtained using equation (iv), for the best curve fitting of the experimental data, is 8.5 (as shown in Figure 5.12(c)).

The up-converted intensity of green band has been monitored at different power density and it shows that the two bands centred at 524 and 548 nm reflect different intensity variation (Shown in Figure 5.13(a). Moreover, the FIR has been monitored as a function of laser input power density at room temperature and it has been observed that variation in these two bands depend on laser input power density (Shown in Figure 5.13 (b)). As B values varies for different sets of samples so equation (iv) can be modified as:

$$\ln\left(\frac{I_{524}}{I_{548}}\right) = \ln B - \frac{\Delta E}{kT} \tag{5.5}$$

where all the terms have their usual meaning as defined above. Similar behaviour was reported $Eu^{3+}/Er^{3+}/Yb^{3+}$ co-doped Y_2O_3 system [Dey, et al. (2014)].
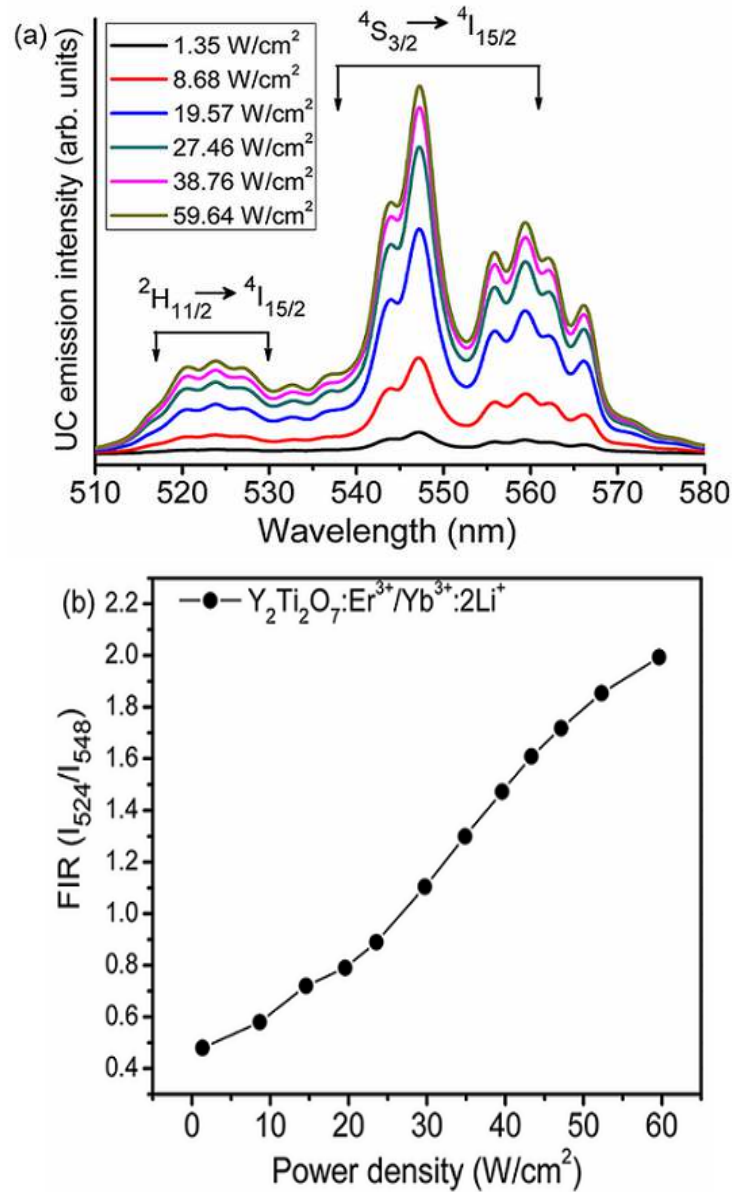

Figure 5.13: (a) Variation in the Up-conversion intensity at different pump power densities and (b) Variation in FIR at different pump power densities at room temperature.

Furthermore, the rate of the change of FIR with respect to temperature is a prominent parameter to demonstrate the utility of the present material as a temperature sensor, termed as sensor sensitivity (S), and defined as [Xu, et al. (2012)]:

$$S = \frac{d(FIR)}{dT} = FIR \times \left(\frac{-\Delta E}{kT^2} \right) \qquad (5.6)$$

where S is the sensor sensitivity & other terms have their usual meanings as defined earlier.

141

The sensor sensitivity was calculated using equation (vi) as a function of the temperatures plotted in Figure 5.13(d). The sensor sensitivity enhanced with increasing sample temperature, thus clearly indicating that this material can be used as a temperature-sensing probe. The maximum sensitivity at 363 K was found to be ~0.0067 K^{-1}. Similar studies have been reported by Dong, et al. (2012) for Er-Mo:$Yb_2Ti_2O_7$ phosphors, with sensitivity of ~0.0074 K^{-1} in the temperature range ~295–610 K. It is worthwhile to compare the sensitivity results of the developed EYYTO:2Li phosphor with similar studies on other materials [Li, et al. (2008), Liu et al. (2011), Rakov, et al. (2012), Li, et al. (2007); Dong, et al. (2007), Leo´n-Luis et al. (2011)]. $Y_2Ti_2O_7$:Er^{3+}/Yb^{3+}:2Li phosphor is a better material for optical sensors both in terms of temperature range and sensor sensitivity. Moreover, the emission intensities of the bands are very stable in the measured temperature range i.e, 298- 673 K, which corroborates its utility at higher temperatures as well. We could not study the performance beyond this temperature range because of instrumental limitations. The results demonstrate that YTO is a good host matrix (melting point ~1600 °C) [Johnson, et al. (2009)] for up-conversion based phosphors, which can be substantially used in display devices and over wide temperature ranges with high-sensitivity temperature sensors.

5.2.1.3 CIE study

The Colour perception of the samples is demonstrated by mathematically defined colour chromaticity diagram (as shown in Figure 5.14).
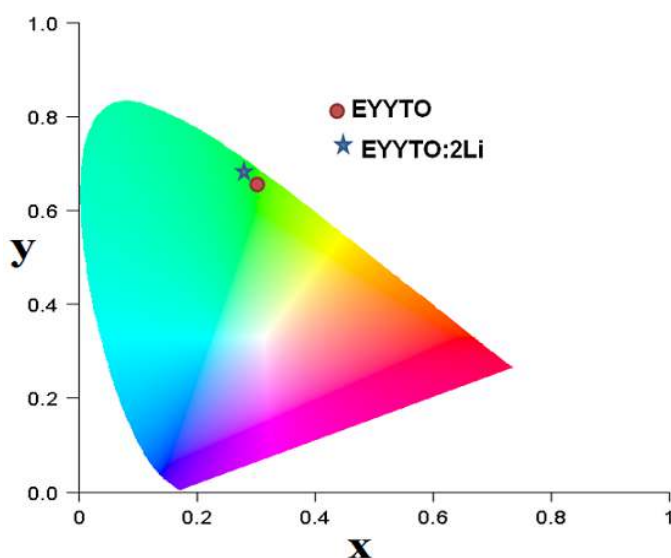

Figure 5.14: CIE diagram for Li$^+$ (0 and 2 at.%) co-doped $Y_2Ti_2O_7$:Er^{3+}/Yb^{3+}.

Clearly, the Commission Internationale de l'Eclairage (CIE) diagram shows that the Li^+-co-doping samples lie towards the pure green region. The typical CIE plots of EYYTO and EYYTO:2Li were calculated, indicating that the Li^+ co-doped phosphors show better improvement in the purity of green colour emitted from the prepared samples.

5.2.1.4 Decay analysis

The decay profile of green band (~548 nm) $^4S_{3/2} \rightarrow {}^4I_{15/2}$ for EYYTO:2Li under 976 nm excitation was measured. Figure 5.15 shows the normalised decay curve of ~548 nm band for the green bands. The decay profile may be well fitted to a mono-exponential function:

$$I = I_0 + A_1 \exp\left(\frac{-t}{\tau}\right) \tag{5.7}$$

where I_0 and I are the initial intensity and intensity at time t, respectively. A_1 is a constant, t is the time, and τ is the decay time of the emitting level. The lifetime of $^4S_{3/2}$ state was found to be ~548 μs, which is higher than that of Li^+-free EYYTO sample ~ 446 μs [Singh, et al.(2013)]. The mono-exponential fitting and its residuals are shown in the Figure inset. The prolonged decay time of EYYTO:2Li can be attributed to the tailored local environment around Er^{3+} ions.
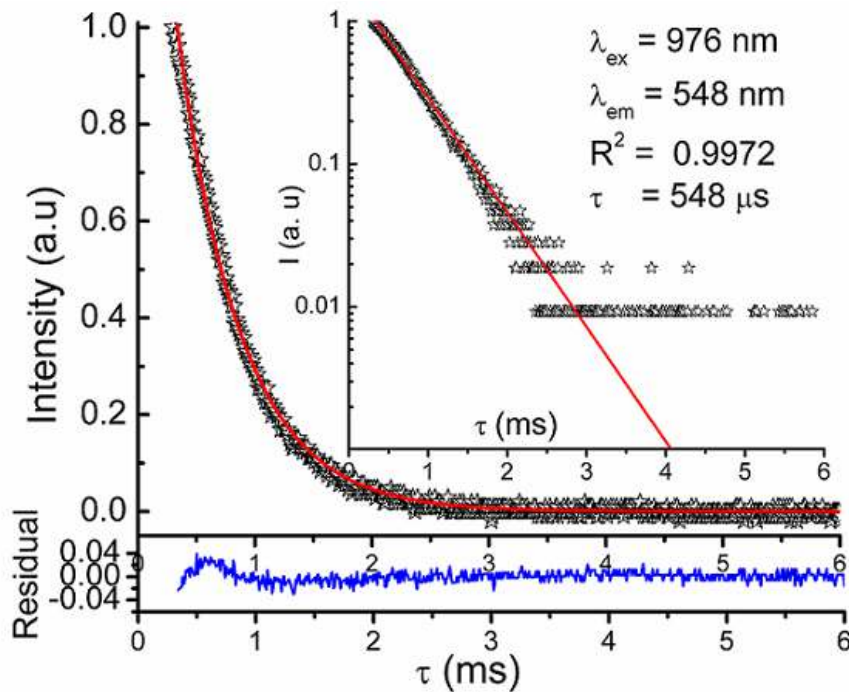

Figure 5.15: Decay curve showing EYYTO:2Li of 548 nm ($^4S_{3/2} \rightarrow {}^4I_{15/2}$) band under 976 nm excitation.

5.5   Conclusions

Li$^+$ co-doped Y$_2$Ti$_2$O$_7$:Er^{3+}/Yb^{3+}phosphors were synthesized by a solid-state ceramic method. The structures of the phosphors were analysed in detail by Rietveld XRD, XPS, FTIR, FE-SEM, Raman and PL measurements. The XRD study confirmed the pyrochlore phase with a fcc structure. The XPS study revealed the characteristic valence states and associated oxygen vacancies on the sample surface. Raman spectroscopy reveals the surface defects associated with the sample and structure corroborates to its pyrochlore type feature. Significantly enhanced green and red emissions were observed after introducing Li$^+$ ions, which may tailor the environment surrounding the Er^{3+} ions. With Li$^+$ ion inclusion, the decay profile of the green bands (548 nm) corroborates the prolonged decay time value as compared to Li$^+$-free sample. The temperature-dependent FIR study corroborates the applicability of this phosphor material in the development of an optical temperature sensor with high sensitivity over a wide temperature range. The maximum sensitivity was found to be ~0.0067 K^{-1} at 363 K. EYYTO:2Li phosphor may be used in the development of an efficient green up-convertor and temperature sensor having a wide temperature range and with high efficacy.

★★★★★★

.